Journal of Power Sources 195 (2010) 4826–4834

Contents lists available at ScienceDirect

Journal of Power Sources

journal homepage: www.elsevier.com/locate/jpowsour

Thermal management of the molten carbonate fuel cell plane

Barbara Bosio[a,*], Danilo Marra[b], Elisabetta Arato[a]

[a] University of Genoa, Faculty of Engineering, Department of Civil, Environmental and Architectural Engineering (DICAT), Italy
[b] Ecole Polytechnique Fédérale de Lausanne, Faculté de l'environnement naturel, architectural et construit (ENAC), Laboratoire d'hydraulique environnementale (LHE), Switzerland

ARTICLE INFO

Article history:
Received 23 October 2009
Received in revised form 26 January 2010
Accepted 13 February 2010
Available online 19 February 2010

Keywords:
Fuel cells
Local temperature distribution
Fluid-dynamics optimisation
Detailed modelling

ABSTRACT

The operating temperature range of molten carbonate fuel cells (MCFCs) is about 925–955 K. An input gas temperature of at least 855 K is necessary to guarantee good ionic conduction inside the cells. Maximum local temperatures higher than 960 K should be avoided because they can cause problems such as electrolyte loss and corrosion.

The first limit can easily be managed, while the second can only be managed through taking many local measurements or, more properly, reliable detailed simulation models.

Using a specific code developed by the authors, the temperature distribution on the cell plane can be calculated with an error of the same order of magnitude as the experimental one.

The study of different MCFC operating conditions carried out using our simulation tool highlighted the difficulties in respecting the constraint on the maximum local temperature.

The temperature maps of an MCFC plane can be very irregular and some parts of the cell can work under critical conditions even if the average temperature is not too high and this aspect is critical for industrial optimisation of MCFC performance.

Different techniques have been tried to obtain a uniform temperature distribution on the cell plane. In particular, having observed that fluid-dynamics plays a predominant role in the problem, a solution based on the use of non-uniform inlet gas-flows has been proposed. The encouraging results obtained will be shown and discussed in detail.

1. Introduction

MCFC plants represent one of the most promising technologies for the production of clean energy and are now close to commercial release.

Plant-run optimisation is fundamental to the refinement of this technology, but can still requires further basic study.

In particular, the process analysis of a 1 MW MCFC hybrid system in Marra and Bosio [1] has shown that one of the more critical features is the local thermal management on the cell plane.

In fact, on the one hand, cell temperature must not be inferior to 855 K in order to guarantee good ionic conduction [2]. On the other hand, maximum local temperatures higher than 960 K on the cell plane have to be avoided for the prevention of cell-component damage, such as electrolyte losses, corrosion of the separator plates, matrix cracking and high temperature creeping of porous components [3,4]. Actually, temperatures should be in the 925–955 K range in order to guarantee high electrical and global efficiencies [5]. Furthermore, temperature distribution on the cell plane should be as uniform as possible because too high a planar temperature gradient could be the cause of component deformation.

Usually, the maximum temperature on the cell plane is the most crucial parameter and it is usually governed by the inlet temperature and the total flow of the cathodic gas. In fact, decreasing the inlet temperature and the total flow of the cathodic gas can lower the maximum temperature. However, these techniques have some limitations and cannot be applied in all cases [2], because of their impact on the management of other operating conditions.

This paper is devoted to the analysis of the mechanisms that determine the temperature distribution on the cell plane: the role of the thermal conductivity and thermal convection exchange-coefficient will be studied through sensitivity analyses. Moreover, having observed that the fluid-dynamics of the anodic and cathodic gases on the cell plane could have a fundamental role in the thermal optimisation, a solution will be proposed based on the use of a non-uniform inlet gas-flow [6].

All these investigations were carried out using the proprietary SIMFC (Simulation of Fuel Cells) code described in chapter 2. The operating conditions reported in Marra and Bosio [1] have been adopted (Table 1).

Rectangular cells with a cross-flow feeding system will be considered.

* Corresponding author. Tel.: +39 010 353 6505; fax: +39 010 353 2589.
E-mail address: barbara.bosio@unige.it (B. Bosio).

0378-7753/$ – see front matter © 2010 Elsevier B.V. All rights reserved.
doi:10.1016/j.jpowsour.2010.02.031

Nomenclature

A	experimental coefficient in local resistance equation in Appendix A [$\Omega\,m^2\,Pa^{2/3}$]
B	experimental coefficient in local resistance equation in Appendix A [K]
c_{iR}	experimental coefficient in local resistance equation in Appendix A [$\Omega\,m^2$]
Cp	specific heat [$J\,mol^{-1}\,K^{-1}$]
d	non-uniform inlet gas pressure coefficient [%]
D	experimental coefficient in local resistance equation in Appendix A [$\Omega\,m^2$]
E	Nernst potential [V]
F	Faraday's constant [$C\,mol^{-1}$]
G	experimental coefficients in local resistance equation in Appendix A [K]
h	coefficient of heat transfer for convection [$W\,m^{-2}\,K^{-1}$]
J	current density [$A\,m^{-2}$]
$J_{H_2,lim}$	limiting current density for the reactant H_2 [$A\,m^{-2}$]
$J_{CO_2,lim}$	limiting current density for the reactant CO_2 [$A\,m^{-2}$]
k	thermal conductivity of the fluid [$W\,m^{-1}\,K^{-1}$];
K	thermal conductivity of the cell packet [$W\,K^{-1}$]
l	passageway height [m]
L_C	characteristic length [m]
M	fluid-dynamic coefficients
N	fluid-dynamic coefficients
n	gas-flow rate per length unit [$mol\,m^{-1}\,s^{-1}$]
n_e	electrons transferred in reactions (1) and (2)
Nu	Nusselt number
p	gas pressure [Pa]
p_{O_2}	partial pressure of the cathodic oxygen
$q_{cross\text{-}over}$	cross-over flow rate [$mol\,s^{-1}$]
Q_{cond}	thermal power density due to conduction [$W\,m^{-2}$]
Q_{reaz}	thermal power density due to reactions [$W\,m^{-2}$]
$Q_{cross\text{-}over}$	thermal power density due to cross-over [$W\,m^{-2}$]
r_i	reaction rate for the ith chemical specie [$mol\,m^{-2}\,s^{-1}$]
r_j	reaction ratio for the jth reaction [$mol\,s^{-1}$]
R	local resistance [$\Omega\,m^2$]
R_g	gas constant [$J\,mol^{-1}\,K^{-1}$]
Re	Reynolds number
s_n	thickness of the nth cell component [m]
s	specific gas/solid interface area ratio
T	gas temperature [K]
T_s	solid temperature [K]
v	gas velocity [$m\,s^{-1}$]
V	cell potential [V]
x,y	cell co-ordinates [m]
w^i	vertical velocity component on the cell plane [$m\,s^{-1}$]
Z	cell geometry, materials and flow regime coefficients

Greek letters

α	cross-over parameter [$N\,m^3\,(atm\,h\,cm^2)^{-1}$]
β	experimental coefficients in local resistance equation in Appendix A
γ	fluid-dynamic coefficients
ΔH	enthalpy variation [$J\,mol^{-1}$]
ΔT	difference between *MAX* and *MIN* temperatures [K]
η_{CONC}	concentration overvoltage [V]
ϑ	friction factor
λ	thermal conductivity [$W\,m^{-1}\,K^{-1}$]
μ	gas viscosity [Pa s]
ν	stoichiometric coefficient
σ	fluid-dynamic coefficients

Subscripts

a	anode
c	cathode
i	ith chemical specie
j	jth reaction
L	longitudinal
n	nth component
T	transversal
MAX	maximum
MIN	minimum
MEAN	mean

The main hypothesis assumed in the present study is that the vertical temperature profile in the cell packet (composed by the separator plate, the top current collector, the anode, the matrix, the cathode and the bottom current collector) is constant [7], i.e. it is assumed that the temperature has the same value in all the components of the cell packet (Fig. 1) and this temperature will be called the solid temperature.

The authors wish to dedicate this paper to the memory of professor Paolo Costa, their sorely missed teacher, who inspired their present work.

2. The SIMFC model

MCFCs were simulated using the detailed proprietary SIMFC (Simulation of Fuel Cells) code, which is based on an electrode micro-model integrated with a 3D macro-model considering local mass, energy, charge and momentum balances on the cell plane and thermal exchanges on the vertical coordinate. The basic equations that determine the MCFC physics are summarised in Appendix A [8–10].

One of the key features of the SIMFC code is an innovative way of taking into account the fluid-dynamics of the anodic and cathodic gases inside the fuel cell. In fact, MCFC simulation models usually consider the current collector gas distributor (CCGD) as composed of many flow-streets that are parallel to each other [6,11–13], while its typical geometry is far from this assumption [14]. For this reason

Table 1
Reference operating conditions.

Fuel cell	
J [$A\,m^{-2}$]	1547
Fuel utilisation [%]	75
Pressure [bar]	3.6
Power [kWel]	500
Cathodic/anodic inlet gas mass flow ratio	37
Cell area [m^2]	0.72
Cell number	300
Inlet anodic gas	
Temperature [K]	873.0
CH_4 mole fraction [%]	2.4
CO mole fraction [%]	6.3
CO_2 mole fraction [%]	7.5
H_2 mole fraction [%]	48.7
H_2O mole fraction [%]	35.2
Inlet cathodic gas	
Temperature [K]	869.0
CO_2 mole fraction [%]	6.8
H_2O mole fraction [%]	8.6
N_2 mole fraction [%]	72.6
O_2 mole fraction [%]	11.9

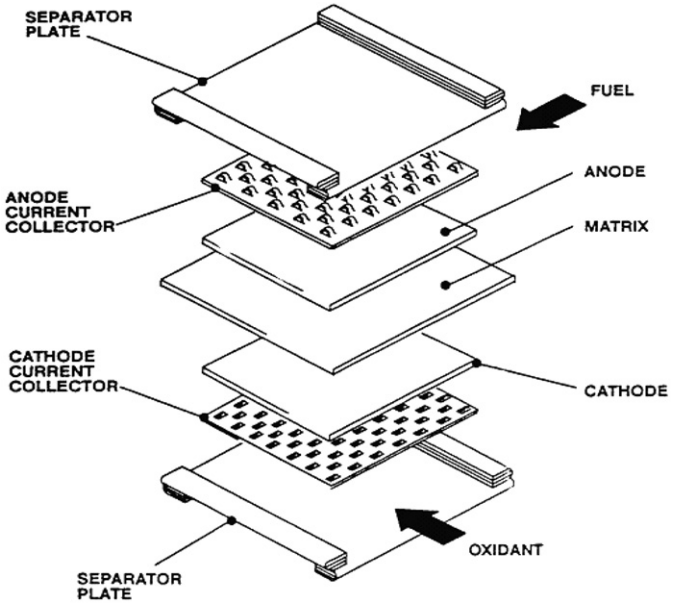

Fig. 1. Reference MCFC cross-flow sketch.

SIMFC considers the specific fluid-dynamic relationships, in terms of dimensionless head losses as a function of the Reynolds number, given by a detailed analysis of the CCGD based on a finite element model [10,15]. This allows the SIMFC code to simulate the gases flowing not only in the principal longitudinal direction, but also in the transversal direction.

The code was validated with experimental data provided by Ansaldo Fuel Cells S.p.A. [16]: the adopted configuration for the comparison was a stack of 150 cells with an area of 0.72 m^2 and a current density of 0.0774 A cm^{-2}. The characteristics of the adopted anodic and cathodic gases are reported in Table 2.

Fig. 2 shows the comparison of the solid temperature map found experimentally and the calculated one using both the detailed fluid-dynamic model (considering the actual CCGD shape) and a simplified one (considering the CCGD as composed of many flow-streets that are parallel to each other).

We can clearly observe that the simulation performed with the use of the detailed fluid-dynamic model gives results that better fit the experimental data in than the simulation based on the simplified fluid-dynamic model, which underestimated the solid temperature map. Both models predict the maximum solid temperature with a minimum relative error (the simplified model underestimates the experimental data by about 1.5%, the detailed one overestimates them by about 0.3%), but the simplified model underestimates the difference between the minimum and maximum solid temperatures by about 32%, while the model that adopts the detailed fluid-dynamic relationships underestimates it by only about 0.5%.

Table 2
Anodic and cathodic gas characteristics.

	Anodic gas	Cathodic gas
Inlet temperature [K]	869	880
Inlet total flow [kmol h^{-1}]	16.845	66.435
Inlet flow of CO [kmol h^{-1}]	0.138	0.0
Inlet flow of CO_2 [kmol h^{-1}]	0.815	5.677
Inlet flow of H_2 [kmol h^{-1}]	3.648	0.0
Inlet flow of H_2O [kmol h^{-1}]	3.517	3.469
Inlet flow of N_2 [kmol h^{-1}]	8.727	46.545
Inlet flow of O_2 [kmol h^{-1}]	0.0	10.744

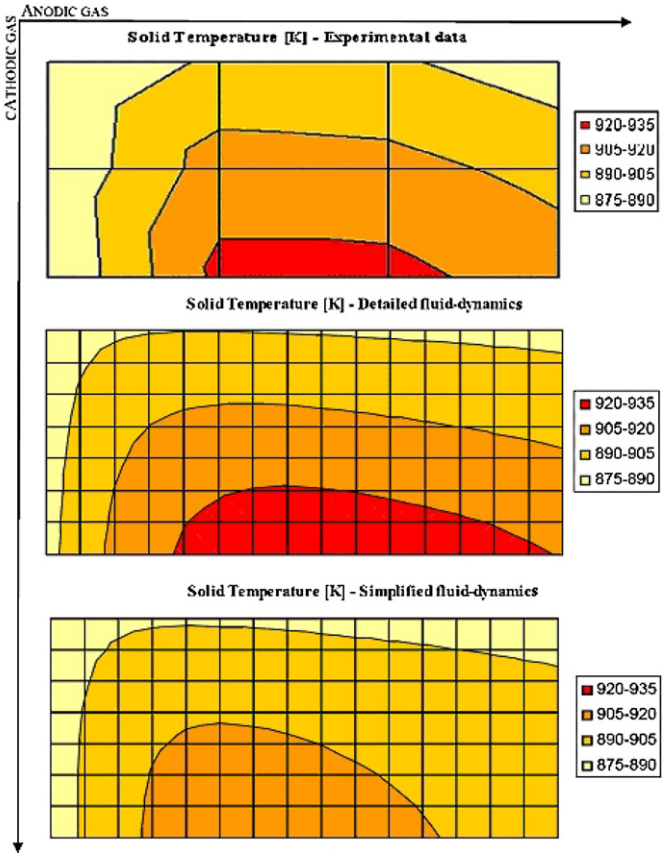

Fig. 2. Maps of the solid temperature [K] measured and simulated with detailed or simplified fluid-dynamic models.

Moreover, considering the mean gas pressure drops, as reported in Table 3, the more appropriate use of the detailed fluid-dynamic relationships allows a better evaluation.

3. The effect of thermal conductivity

In this section we have investigated the role of the thermal conductivity K [WK^{-1}] of the cell packet (plate + collector + anode + matrix + cathode + collector) with parametric analyses.

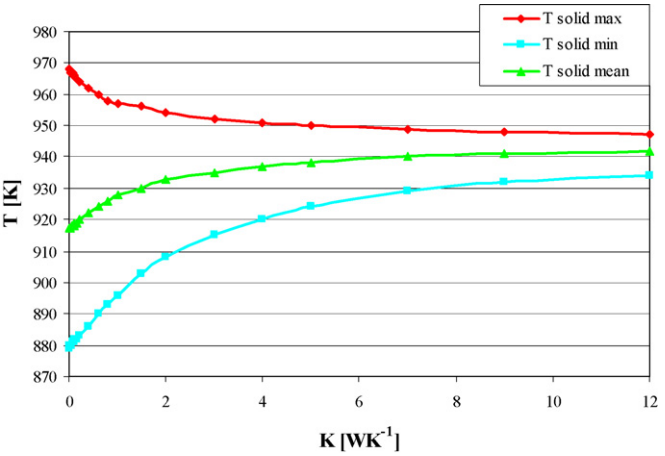

Fig. 3. Minimum, maximum and average solid temperatures [K] vs. thermal conductivity K [WK^{-1}].

Table 3
Mean anodic and cathodic gas pressure drops [mbar] measured and simulated with detailed and simplified fluid-dynamic models.

	Experimental data	Detailed fluid-dynamics	Simplified fluid-dynamics
Mean anodic gas pressure drop [mbar]	−6.42	−7.19	−5.51
Mean cathodic gas pressure drop [mbar]	−4.90	−6.33	−10.54

Fig. 3 shows that when K increases the minimum and maximum solid temperatures tend to converge to the same asymptotic value, but involve an increase in the average temperature.

In Fig. 3 we can see that the difference between the minimum and maximum solid temperatures decreases while K increases. We can also note that the steepest decrease in the temperature difference is for K between $0\,W\,K^{-1}$ and $1\,W\,K^{-1}$, while with any further increase in K the decrease of temperature difference becomes flatter and flatter.

Consequently, as we can note from Fig. 4, which shows the solid temperature maps on the cell plane for thermal conductivity values equal to $0.117\,W\,K^{-1}$, $1\,W\,K^{-1}$ and $5\,W\,K^{-1}$, respectively, if K increases the temperature map becomes ever more uniform.

Then, we calculated the value of K that, on the basis of the thickness s_n and the thermal conductivity λ_n of each typically adopted cell component n, should distinguish the cell packet if all the conductivities are assumed to be in parallel; so we used the relationship:

$$K = \sum_{n=1}^{6} s_n \lambda_n$$

The value of K obtained is $0.075\,W\,K^{-1}$, very close to the one usually adopted to best fit the experimental results, i.e. $K = 0.117\,W\,K^{-1}$ [16]. Nevertheless, some experiments showed that if a plate thickness of 2 cm was adopted the situation did not notably change with respect to the standard case where the plate thickness was of the order of 0.03 cm, even though we expected a sensible increase in the thermal conductivity ($K = 0.528\,W\,K^{-1}$) and consequently a more uniform temperature map [16]. The reason for this disagreement could be in the hypothesis of thermal conductivities in parallel. We could assume that the conductivities are in series, using the relationship

$$\frac{1}{K} = \sum_{n=1}^{6} \frac{1}{s_n \lambda_n}$$

and obtaining $K = 0.0010\,W\,K^{-1}$ and $K = 0.0012\,W\,K^{-1}$ for the reference case when the plate is 2 cm.

A more reliable assumption could be that the metallic components of the cell packet (plate and collector) are in parallel, while the other components are in series: this would lead to $K = 0.0016\,W\,K^{-1}$ (for the reference case) and $K = 0.0018\,W\,K^{-1}$ (when the plate is 2 cm thick).

These two assumptions (conductivities in series and conductivities in parallel-series) seem to explain why a thicker plate does not significantly change the temperature map: K is not significantly increased, different from what happens if the conductivities are considered in parallel.

Moreover, if we study Fig. 5 that represents a zoom of Fig. 3 for $0\,W\,K^{-1} \le K\,W\,K^{-1} \le 0.2\,W\,K^{-1}$, we can note that a variation of K in the selected range does not notably change the temperatures. This explains the fact that, for the reference situation, we do not encounter any differences in temperature maps

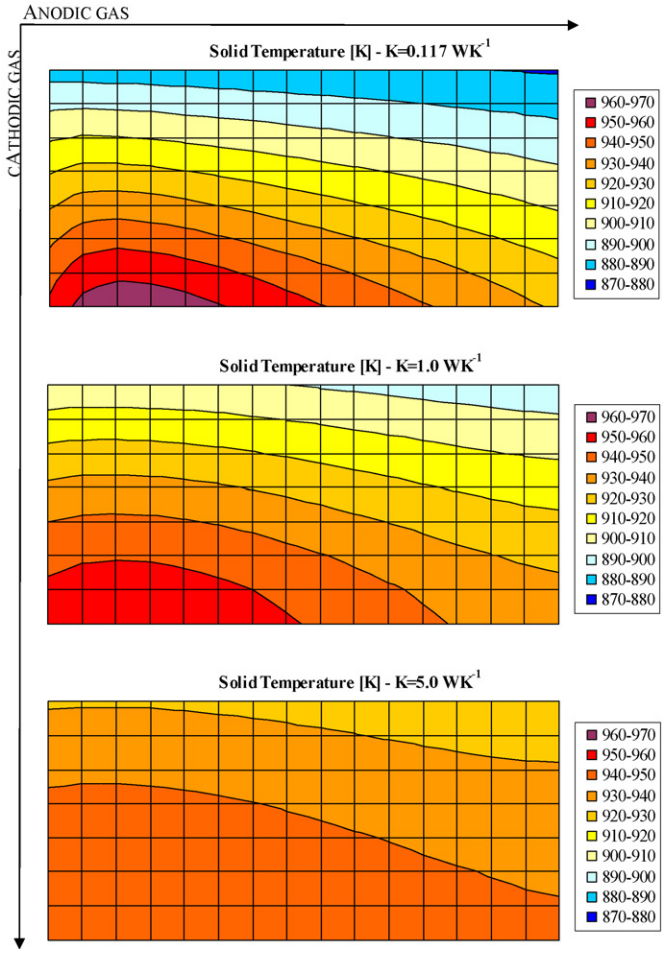

Fig. 4. Solid temperature [K] maps on the cell plan, for K equal to $0.117\,W\,K^{-1}$, $1\,W\,K^{-1}$ and $5\,W\,K^{-1}$.

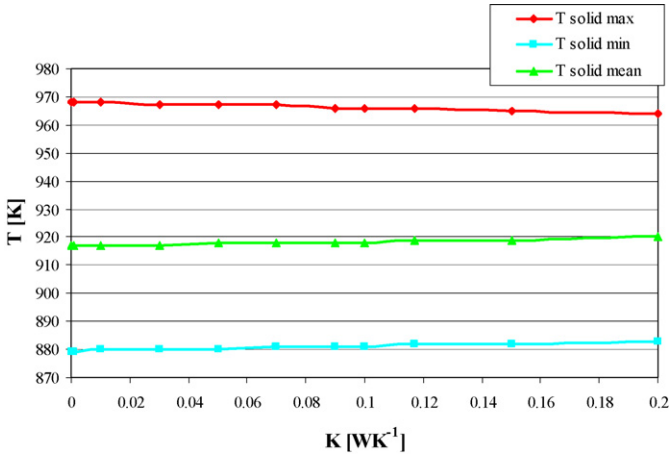

Fig. 5. Minimum, maximum and average solid temperatures [K] for $0\,W\,K^{-1} \le K\,W\,K^{-1} \le 0.2\,W\,K^{-1}$.

between the evaluated K (despite different ways in the evaluation: parallel, series, parallel + series) and the one usually adopted ($K = 0.117\ \mathrm{W\,K^{-1}}$).

Bearing these considerations in mind, the question is how we can increase K to obtain sufficient high values to make the temperature map more uniform (for example K higher than $2\ \mathrm{W\,K^{-1}}$).

We can act only on s_n and λ_n. Dealing with s_n we have already observed that a sensible increase in the plate thickness does not change the temperature map: this can be extended also to the other components whose thickness is moreover limited by the requirements for proper electrochemical functioning. Acting on λ_n means a material change and although many studies have been devoted to the search for and development of new materials [17–22], materials with the desired thermal characteristics for use as cell components have not be found yet. Moreover, having established that the thermal conductivity of the cell components is in series (or in series + parallel), an increase of some λ_n does not produce a high enough increase in K.

4. The effect of thermal convection

In this section we have investigated the manner in which the gas coefficient of heat transfer for convection, h [$\mathrm{W\,m^{-2}\,K^{-1}}$], affects cell temperature distribution. In the simulations performed with the SIMFC code, h was estimated from the dimensionless heat transfer parameter, the Nusselt number Nu.

In order to best fit the experimental evidence on the temperature, Nu is normally taken as equal to 3 [23–27]: this leads to very high values of h (about $390\ \mathrm{W\,m^{-2}\,K^{-1}}$ for the anodic gas and $220\ \mathrm{W\,m^{-2}\,K^{-1}}$ for the cathodic gas).

A parametric analysis of Nu was carried out: we considered values of Nu in the range 0–5, although we must emphasise that Nu less than 1 in this context is not applicable because it means that the gases are almost stationary.

Fig. 6 shows the graphs of maximum, minimum and average solid temperatures and the average anodic and cathodic gas outlet temperatures as a function of the Nu.

In the figure we can note that, for Nu greater than 1.5, the reported quantities have reached the asymptotic values that correspond to their minimum, except for the mean anodic gas outlet temperature that is at its maximum. This fact demonstrates that for Nu > 1.5 the heat transfer phenomenon is already under convection regime and a further increase of Nu will not change the temperature.

Furthermore, Fig. 6 also shows that for very low values of Nu the average anodic and cathodic gas outlet temperatures tend to coincide, while the average solid temperature reaches its maximum value. In addition, as Nu increases, the difference between the maximum and minimum solid temperatures increases, reaching its maximum asymptotic value for Nu > 1.5: this suggests that the temperature distribution on the cell plane becomes ever more non-uniform as Nu increases.

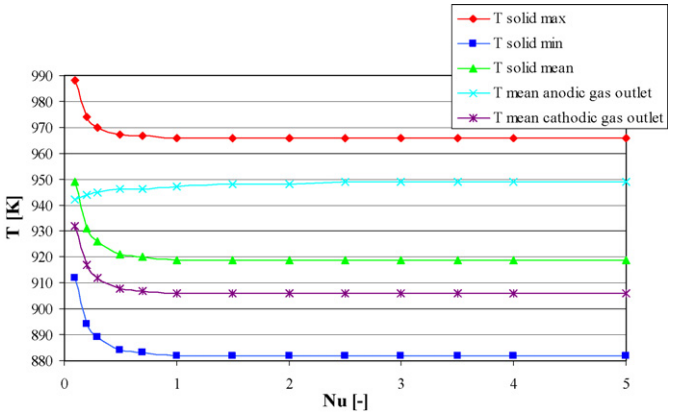

Fig. 6. Minimum, maximum and average solid temperatures [K] and average anodic and cathodic gas outlet temperatures [K] vs. Nu.

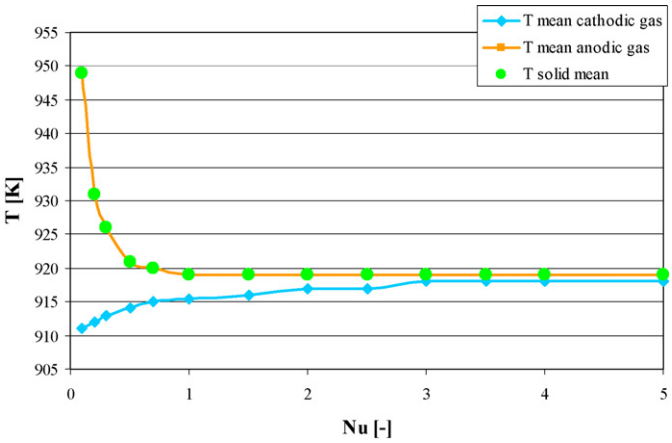

Fig. 7. Average solid, anodic and cathodic gas temperatures [K] vs. Nu.

An increase in Nu is always followed by a decrease in the mean solid and anodic gas temperature, as is shown in Fig. 7. This figure, moreover, demonstrates that under our operative conditions (a cathodic flow much higher than the anodic one, as is shown in Table 1) the average solid temperature has the same value as the average anodic gas one for any values of Nu and, when Nu increases (in particular for Nu > 3), such temperatures tend to coincide with the average cathodic gas temperature.

Such results demonstrate that the thermal behaviour of the cell is mainly governed by the gases: in fact, already at low Nu values (i.e. low convection heat transfer coefficients for the gases) the anodic and cathodic gases and the solid have the same average temperature. As the gases are mainly responsible of the temper-

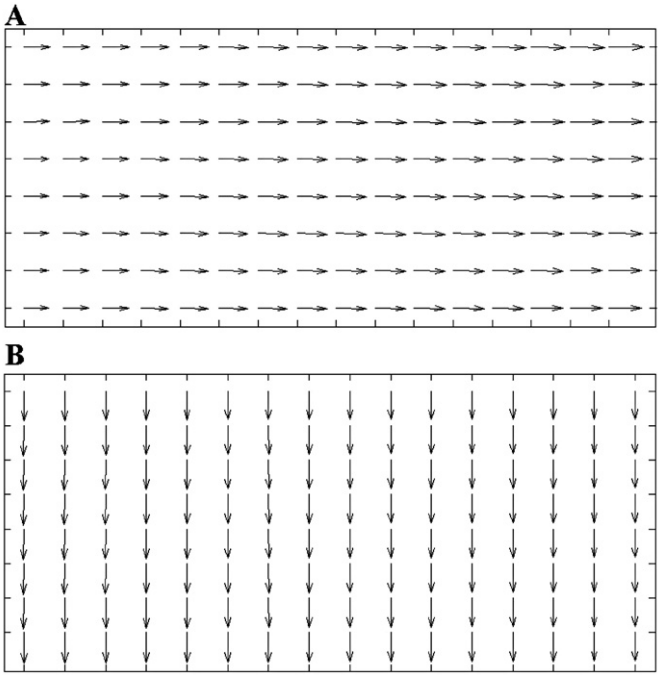

Fig. 8. Reference velocity maps for the anodic (A) and cathodic (B) gases obtained for uniform inlet gas pressure profiles.

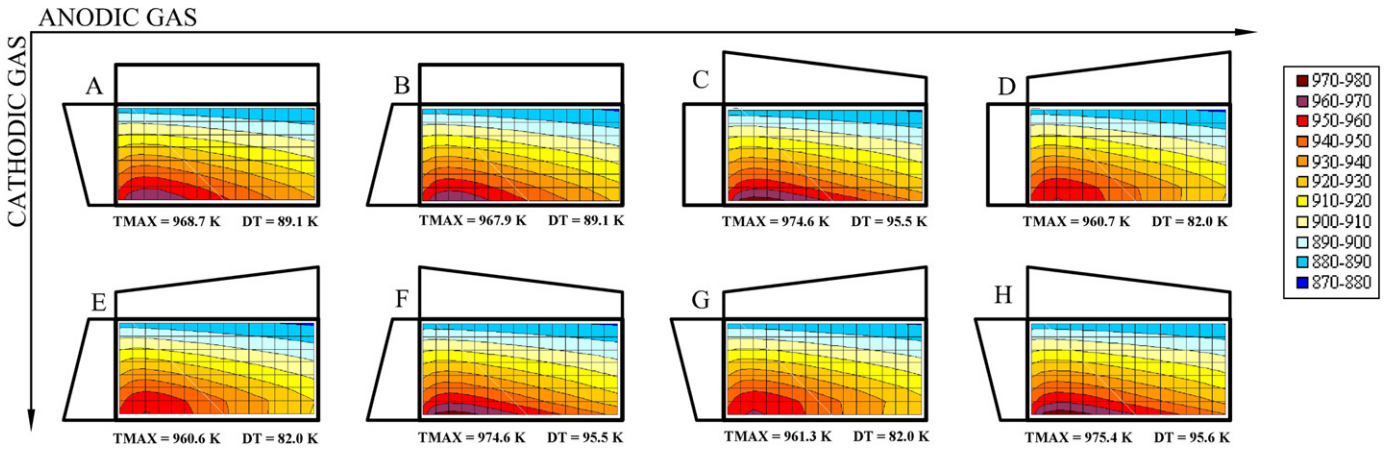

Fig. 9. Temperature maps for the different patterns if $d = 0.005\%$.

ature distribution on the cell plane it is possible to deduce that their fluid-dynamic behaviour is strongly involved in the thermal management of the cell.

5. The effect of the inlet gas distribution

As has been observed, the gas fluid-dynamics has a fundamental role in the thermal behaviour of the fuel cells. In this section we have investigated the possibility of modifying the gas fluid-dynamics to optimise the temperature map. The easiest proposed solution for tackling the problem is to modify the anodic and cathodic gas inlet flow distributions. The interesting work of Liu et al. [6] – whose model considers the CCGD as composed of many flow-streets that are parallel to each other – proposes an inlet flow distribution that, increasing the non-uniformity of the longitudinal velocity, affects the temperature map. With the use of the SIMFC code, where the specific fluid-dynamic relationships for the adopted CCGD are implemented [1], it is possible to evaluate how a non-uniform flow feed also produces higher velocity components which are transversal to the main flow direction, so that there is further feedback to the cell temperature distribution.

Fig. 8 shows the reference velocity maps for the anodic and cathodic gases obtained for uniform inlet gas pressure profiles.

From a first glance at Fig. 8 it can be observed that the main component of the velocity of the anodic and the cathodic gases is along the principal direction. In particular, its mean value is 2.66 m s^{-1} for the cathodic gas and 0.41 m s^{-1} for the anodic one, its maximum value is 2.84 m s^{-1} for the cathodic gas and 0.48 m s^{-1} for the anodic one, and its minimum value is 2.54 m s^{-1} for the cathodic gas and 0.33 m s^{-1} for the anodic one. Despite that, a non-null transversal component appears: the percentage ratio of its maximum value to the maximum value of the longitudinal component is about 3.3% for the anodic gas and 3.8% for the cathodic one.

Our investigations consider, in line with Liu et al. [6], uniform inlet gas pressure profiles, progressively linearly decreasing profiles, and progressively linearly increasing profiles combined to build eight non-uniform inlet flow patterns, as shown in Fig. 9.

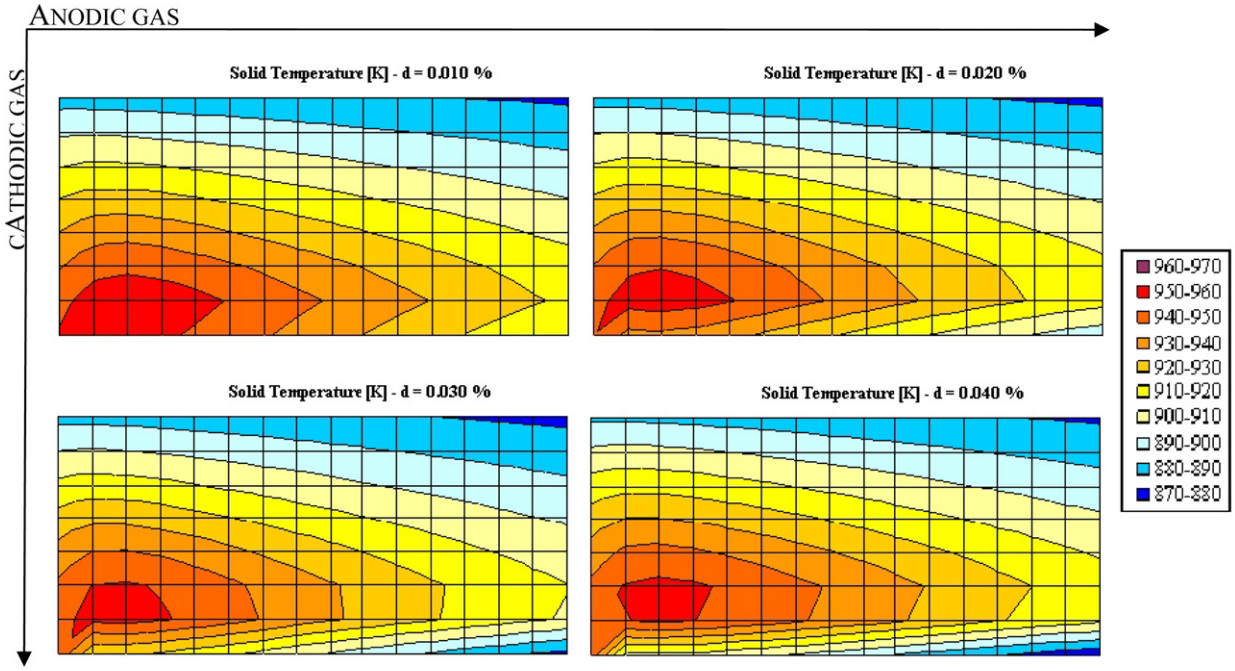

Fig. 10. Pattern D: temperature maps [K] if $d = 0.010\%$, 0.020%, 0.030%, 0.040%.

Table 4
Temperature [K] results for the different patterns of Fig. 8 if $d = 0.005\%$.

	T^{MAX}	T^{MIN}	T^{MEAN}	ΔT	% T^{MAX}	% T^{MIN}	% T^{MEAN}	% ΔT
Ref. Cond.	968.0	878.9	917.2	89.1	–	–	–	–
A	968.7	879.6	918.4	89.1	0.07	0.08	0.13	0.00
B	967.9	878.8	917.0	89.1	−0.01	−0.01	−0.02	0.00
C	974.6	879.1	918.6	95.5	0.68	0.02	0.15	7.18
D	960.7	878.7	915.7	82.0	−0.75	−0.02	−0.16	−7.97
E	960.6	878.6	915.6	82.0	−0.76	−0.03	−0.17	−7.97
F	974.6	879.1	918.5	95.5	0.68	0.02	0.14	7.18
G	961.3	879.3	916.7	82.0	−0.69	0.05	−0.05	−7.97
H	975.4	879.8	919.8	95.6	0.76	0.10	0.28	7.30

The reference temperature map, with which we will compare the different chosen pattern temperature results, is the previous one obtained with a uniform constant inlet anodic and cathodic gas pressure (Fig. 4 assuming $K = 0.117\,W\,K^{-1}$).

Fig. 9 shows the temperature maps for the eight different patterns for $d = 0.005\%$, where d represents the unilateral deviation of the non-uniform profile, which is the ratio between the variation in the inlet gas pressure on one side (0.18 mbar) and the mean inlet gas pressure (3.6 bar).

Comparing the different temperature distributions we can observe that: the temperature maps of patterns A and B are quite similar to the reference case; the maps of patterns C, F and H are worse; and the maps of patterns D, E and G are more uniform with a lower maximum temperature. The main variations are given by the cathodic inlet gas distribution, whereas the anodic one does not affect the maps: in fact the same temperature distributions are given by patterns A and B, patterns C, F and H, and patterns D, E and G. This suggests that only the cathode gas influences the temperature distribution on the cell plane because its flow rate exceeds that of the anode gas [6], as shown in Table 1.

Table 4 shows the results of the analysis reported in Fig. 9 in terms of minimum, maximum and mean solid temperature (T^{MAX}, T^{MIN}, T^{MEAN}), difference between minimum and maximum solid temperature (ΔT), percentage variation with respect to the reference case of T^{MAX}, T^{MIN}, T^{MEAN} and ΔT (% T^{MAX}, % T^{MIN}, % T^{MEAN} and % ΔT).

In Table 4 we can observe that patterns D, E and G give a T^{MAX} reduction of about 0.7% and a ΔT reduction of about 8%: this means that the temperature map is more uniform with a lower peak. On the other hand, patterns C, F and H produce less uniform temperature maps with higher peaks: T^{MAX} increases of about 0.7% and ΔT increases of about 7%. Moreover, as discussed above, the D, E and G pattern results are about the same, so that we chose pattern D as the best one for the temperature management, considering that with this configuration it is possible to maintain a uniform constant anodic gas inlet pressure and vary only the cathodic one.

Fig. 10 shows the temperature maps for pattern D for different d.

When d increases the temperature peak decreases and moves away from the bottom left corner. Moreover, as underlined by Fig. 11, as d increases T^{MIN} and T^{MEAN} also decrease slightly. In general, the minimum temperature is always acceptable (>855 K), but not ideal (>925 K).

Fig. 12 demonstrates that the variation of ΔT decreases rapidly when d is increased up to 0.03%, while it starts to increase again for higher values of d. For this reason the optimal configuration for the temperature distribution on the cell plane could be identified in pattern D with $d = 0.03\%$, which would seem to be the best compromise between the uniformity of the map and the lower T^{MAX}.

In Fig. 13 the velocity maps of the anodic and cathodic gases obtained for pattern D with $d = 0.03\%$ are reported. In this case the transversal component of the velocity is more relevant than the reference case one (Fig. 8), for both the anodic and the cathodic gases: now the percentage ratio between the minimum and maximum values of the longitudinal component is about 6.2% for the anodic gas and 9.7% for the cathodic one. This underlines the fact that, although the anodic gas inlet flow is constant, the inlet velocity profile of the cathodic gas indirectly also affects the anodic gas velocity map, in particular its transversal component, altering gas densities and viscosities [1,15,16]. Finally, the main component of the velocity has a mean value of 2.65 m s^{-1} for the cathodic gas and 0.40 m s^{-1} for the anodic one, the maximum value is 2.77 m s^{-1} for the cathodic gas and 0.47 m s^{-1} for the anodic one, and the minimum value is 2.54 m s^{-1} for the cathodic gas and 0.33 m s^{-1} for the anodic one: comparing these values with the reference condition ones and observing that they are really similar, we can conclude that the proposed solution mainly affects the transversal velocity components rather than the longitudinal ones.

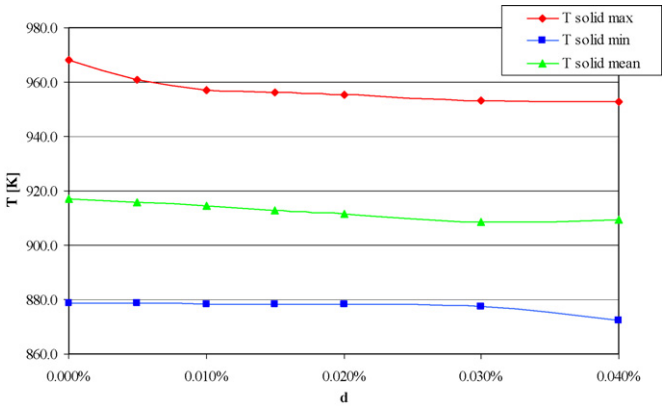

Fig. 11. Pattern D: minimum, maximum and mean solid temperatures [K] vs. d [%].

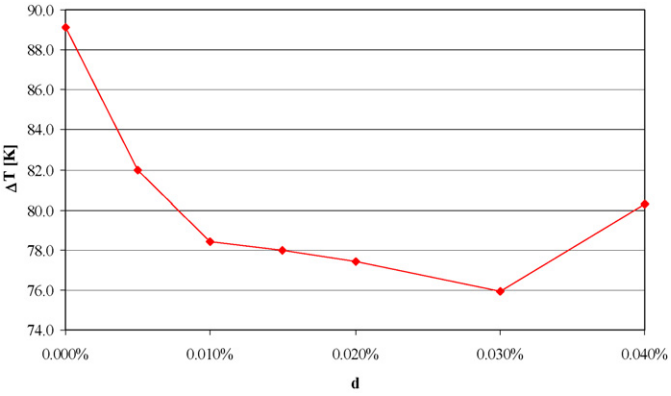

Fig. 12. Pattern D: difference between minimum and maximum solid temperatures [K] vs. d [%].

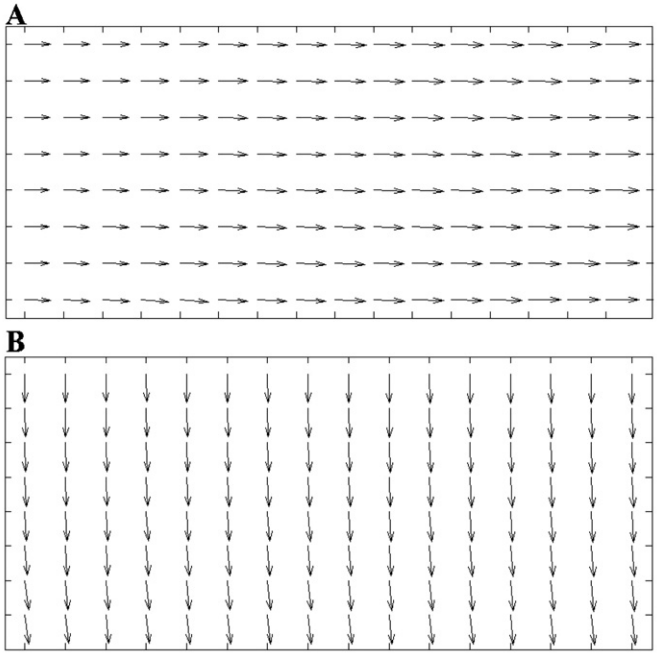

Fig. 13. Velocity maps for the anodic (A) and cathodic (B) gases obtained for pattern D if $d = 0.03\%$.

6. Conclusions

This paper presents the analyses of some of the mechanisms that govern the temperature distribution on the cell, which is one of the key features for the correct functioning of MCFCs. Thanks to the simulations performed with the detailed proprietary SIMFC model, whose results have been validated by experimental tests, we have been able to investigate the role of the thermal conductivity of the cell and the thermal convection of the gases on the temperature map. The analysis has shown how an increase in the thermal conductivity (K) gives a more uniform temperature map with a lower maximum value; however, the increase in K that has been evaluated as necessary would involve component thermal characteristics that are still not available.

The investigation of the thermal convection of the gases, carried out with a parametric analysis on Nu, has shown that in the reference operative conditions ($Nu = 3$) the heat transfer for convection has already achieved its maximum potential. Moreover, the thermal behaviour of the cell appeared to be governed mainly by the gas fluid-dynamics. For this reason we investigated the possibility of optimising the temperature map by changing the gas fluid-dynamics by modifying the profile of the inlet gas pressures.

From the different patterns studied we chose a solution where the anodic gas inlet pressure is constant while the cathodic one has a progressively linear increasing, guaranteeing both the minimum temperature peak and the minimum ΔT on the cell plane.

The proposed solution, which can be realised by the use of appropriate cathodic inlet manifolds, has the advantage of providing a temperature map optimisation without the need to modify the key cell components, the gas compositions, the fuel utilisation or the load [1]: this is very important because it can guarantee the same plant efficiency [28], while maintaining the temperature in the acceptable range for the correct utilisation of the cells.

Acknowledgements

This work has been supported by ISAB Energy Services - ERG Group, within the framework of a financed research project. The authors wish to thank Mario Abela and Luigi Iannitti (ISAB Energy Services – ERG Group) and Mauro Rovatti (DICheP, University of Genoa) for the project management.

The authors wish also to thank Roberta Massa and Filippo Parodi of Ansaldo Fuel Cells for the data placed at disposal for the PhD thesis of Danilo Marra.

Appendix A. Basic equations governing SIMFC

- Reactions

$$H_2 + CO_3^{2-} \rightarrow H_2O + CO_2 + 2e^- \quad (1)$$

$$CO_2 + 1/2\,O_2 + 2e^- \rightarrow CO_3^{2-} \quad (2)$$

$$CO + H_2O \rightarrow CO_2 + H_2 \quad (3)$$

$$H_2 + 1/2\,O_2 \rightarrow H_2O \quad (4)$$

$$CO + 1/2\,O_2 \rightarrow CO_2 \quad (5)$$

- Mass balances
  - Anodic gas

$$\frac{\partial n_i}{\partial x} = r_i \text{ where } r_i = \sum_{j=2}^{5} \nu_{i,j} r_j \text{ and } r_2 = \frac{J}{n_e F}$$

  - Cathodic gas

$$\frac{\partial n_i}{\partial y} = r_i \text{ where } r_i = \nu_{i,1} r_1 + \sum_{j=4}^{5} \nu_{i,j} r_j \text{ with } r_1 = r_2$$

  - Gas cross-over

$$q_{cross-over} = \alpha\,|p_a - p_c|$$

- Energy balances
  - Anodic gas

$$\sum_i n_i Cp_i \frac{\partial T_a}{\partial x} = \sum_i \frac{\partial n_i}{\partial x} \int_{T_a}^{T_s} Cp_i dT_a + S_a h_a (T_s - T_a) + Q_{cross\text{-}over}$$

$$\text{if } p_a < p_c \;\; Q_{cross\text{-}over} = -\sum_j r_j \Delta H_j \text{ with } j = 4$$

$$\text{else } Q_{cross\text{-}over} = 0$$

  - Cathodic gas

$$\sum_i n_i Cp_i \frac{\partial T_c}{\partial y} = \sum_i \frac{\partial n_i}{\partial y} \int_{T_c}^{T_s} Cp_i dT_c + S_c h_c (T_s - T_c) + Q_{cross\text{-}over}$$

$$\text{if } p_a > p_c \;\; Q_{cross\text{-}over} = -\sum_j r_j \Delta H_j \text{ with } j = 4, 5$$

$$\text{else } Q_{cross\text{-}over} = 0$$

  - Solid

$$S_a h_a (T_s - T_a) + S_c h_c (T_s - T_c) = Q_{cond} + Q_{reaz}$$

$$\text{where } Q_{cond} = \sum_n (s_n \lambda_n) \left(\frac{\partial^2 T_s}{\partial x^2} + \frac{\partial^2 T_s}{\partial y^2} \right)$$

$$\text{and } Q_{reaz} = \sum_{j=1}^{3} r_j \Delta H_j - VJ$$

- Momentum balances
  - Simplified fluid-dynamics

$$\text{Anodic gas : } \frac{\partial p_a}{\partial x} = Z_a \frac{\mu_a \nu_a}{l^2}$$

$$\text{Cathodic gas : } \frac{\partial p_c}{\partial y} = Z_c \frac{\mu_c \nu_c}{l^2}$$

  - Detailed fluid-dynamics

Anodic gas–longitudinal flow :

$$\vartheta_{a,L} = M_L \mathrm{Re}_{a,L}^{\gamma_L} - \frac{w^i}{w_{MAX}} N_{a,L} \mathrm{Re}_{a,L}^{\sigma_{a,L}}$$

Anodic gas–transversal flow :

$$\vartheta_{a,T} = M_T \mathrm{Re}_{a,T}^{\gamma_T} - \frac{w^i}{w_{MAX}} N_{a,T} \mathrm{Re}_{a,T}^{\sigma_{a,T}}$$

Cathodic gas–longitudinal flow :

$$\vartheta_{c,L} = M_L \mathrm{Re}_{c,L}^{\gamma_L} - \frac{w^i}{w_{MAX}} N_{c,L} \mathrm{Re}_{c,L}^{\sigma_{c,L}}$$

Cathodic gas–transversal flow :

$$\vartheta_{c,T} = M_T \mathrm{Re}^{\gamma_T} - \frac{w^i}{w_{MAX}} N_{c,T} \mathrm{Re}_{c,T}^{\sigma_{c,T}}$$

- Electrochemical kinetics
  - Cell voltage
    $V = E - RJ - \eta_{CONC}$
  - Nernst voltage
    $$E = \frac{-\Delta G}{n_e F} = \frac{-\Delta G_0}{n_e F} - \frac{RT_s}{n_e F} \ln\left(\prod_i p_i^{\nu_i}\right)$$
  - Local resistance
    $$R = A \frac{e^{B/T}}{p_{O_2}^{\beta}} + c_{iR} + De^{G/T_S}$$
  - Concentration overvoltage
    $$\eta_{CONC} = \frac{R_g T}{n_e F}\left[\ln\left(1 - \frac{J}{J_{H_2,\lim}}\right) + \frac{J}{J_{H_2,\lim}} + \ln\left(1 - \frac{J}{J_{CO_2,\lim}}\right) + \frac{J}{J_{CO_2,\lim}}\right]$$

References

[1] D. Marra, B. Bosio, Int. J. Hydrogen Energy 32 (2007) 809–818.
[2] E. Arato, B. Bosio, R. Massa, F. Parodi, J. Power Sources 86 (2000) 302–308.
[3] F.J. Perez, M.P. Hierro, D. Duday, C. Gomez, M. Romero, L. Daza, Oxid. Met. 53 (2000) 376–398.
[4] J.P.P. Huijsmans, G.J. Kraaij, R.C. Makkus, G. Rietveld, E.F. Sitters, H.T.J. Reijers, J. Power Sources 86 (2000) 117–121.
[5] S.F. Au, S.J. McPhail, N. Woudstra, K. Hemmes, J. Power Sources 122 (2003) 37–46.
[6] S.F. Liu, H.S. Chu, P. Yuan, J. Power Sources 161 (2006) 1030–1040.
[7] H. Xi, J. Sun, V. Tsourapas, J. Power Sources 165 (2007) 253–266.
[8] B. Bosio, P. Costamagna, F. Parodi, Chem. Eng. Sci. 54 (1999) 2907–2916.
[9] B. Bosio, P. Costamagna, E. Arato, P. Costa, in: S.G. Pandalai (Ed.), Recent Research Developments in Electrochemistry, Transworld Research Network, Trivandrum, Kerala (India), 2002, pp. 21–45.
[10] D. Marra, B. Bosio, E. Arato, Chem. Eng. Process. 483 (2009) 797–807.
[11] G. De Simon, F. Parodi, M. Fermeglia, R. Taccani, J. Power Sources 115 (2003) 210–218.
[12] Y.R. Lee, M.J. Yoo, G.Y. Chung, H.C. Lim, T.H. Lim, S.W. Nam, S.A. Hong, Korean J. Chem. Eng. 22 (2005) 219–227.
[13] M. Baranak, H. Atakül, J. Power Sources 172 (2007) 831–839.
[14] M. Katz, S.P. Bonk, D.L. Maricle, M. Abrams, Fuel cell current collector, United States Patent, International Fuel Cells Corporation, 1991, Patent Number: 4983472.
[15] D. Marra, Int. J. Hydrogen Energy 33 (2008) 3173–3177.
[16] D. Marra, Fluid-dynamic characterisation of Molten Carbonate Fuel Cells in plant optimization, PhD Thesis, University of Genoa, Department of Civil, Environmental and Architectural Engineering (DICAT), 2008.
[17] C. Milanese, V. Berbenni, G. Bruni, A. Marini, G. Chiodelli, M. Villa, J. Power Sources 177 (2006) 1893–1896.
[18] M.J. Escudero, L. Mendoza, M. Cassir, T. Gonzalez, L. Daza, J. Power Sources 160 (2006) 775–781.
[19] M.H. Kim, M.Z. Hong, Y.S. Kim, E. Park, H. Lee, H.W. Ha, K. Kim, Electrochim. Acta 51 (2006) 6145–6151.
[20] H. Colon-Mercado, P. Ganesan, B. Popov, Surf. Coat. Technol. 201 (2007) 6452–6459.
[21] S. Randström, C. Lagergren, P. Capobianco, J. Power Sources 160 (2006) 782–788.
[22] E. Simonetti, R. Lo Presti, J. Power Sources 160 (2006) 816–820.
[23] J.H. Koh, H.K. Seo, Y.S. Yoo, H.C. Lim, Chem. Eng. J. 87 (2002) 367–379.
[24] P. Greppi, B. Bosio, E. Arato, Int. J. Hydrogen Energy 33 (2008) 6327–6338.
[25] C. Tomasi, M. Baratieri, B. Bosio, E. Arato, P. Baggio, J. Power Sources 157 (2006) 765–774.
[26] F. Yoshiba, N. Ono, Y. Izaki, T. Watanabe, T. Abe, J. Power Source 71 (1998) 328–336.
[27] F. Yoshiba, T. Abe, T. Watanabe, J. Power Source 87 (2000) 21–27.
[28] B.S. Kang, J.H. Koh, H.C. Lim, J. Power Sources 108 (2002) 232–238.